Deformation Field of Limestone Specimen under Uniaxial Compression Loads Using Video Images

Jinming Xu, Deming Li, and Huiting Fang

Abstract. The original images were obtained from the uniaxial compression tests of limestone and transformed into the static and responding grayscale ones. The displacement field was computed using the particle image velocimetry technique. The strains were obtained from the displacements using the local least square method and investigated at different locations. It was found that the deformation changes steadily followed by a rapid increase as time passes and only a few of them had been developed into the visible cracks, although several deformation concentrations occurred in the specimen under the compression loads. The techniques presented herein provide valuable information in investigating the failure mechanism of the rock materials.

1 Introduction

The deformation features of rock materials play an important role in practice. With the development of the computer techniques, these features have been explored using the digital image analysis, permitting a fast and accurate acquisition of information of the rock materials. For example, Deb et al [3] recommended a digital face mapping method to characterize rock mass exposures; Yin et al [6] utilized the sequential images of geomaterials to obtain the locations of cracks; Xu et al [5] obtained the displacement field using a digital image correlation technique;

Jinming Xu · Deming Li
Department of Civil Engineering, Shanghai University, Shanghai, China
e-mail: xjming@163.com

Huiting Fang
Shanghai Science and Technology Museum, Shanghai, China
e-mail: fanghuiting85@163.com

Z. Qian et al. (Eds.): Recent Advances in CSIE 2011, LNEE 129, pp. 547–552.
springerlink.com

Chen et al [2] obtained the strains of a deformed square grids; White et al [4] developed a deformation measurement system based on particle image velocimetry (PIV); Bouaynaya and Schonfeld [1] investigated the performance of motion-based particle filters for object tracking in video sequences.

In the current study, the PIV method was used to investigate the full-field displacements and strains on the specimen surface under external loads from the video images captured in the uniaxial compression tests.

2 Computation of Displacement Field

2.1 Laboratory Tests and Image Acquisition

The limestone was obtained from the Baiheling slope, located in Huzhou City, Zhejiang Province, China. The rock was sliced into the cubic specimens in a size of around 50 × 50 × 50 mm. The uniaxial compression tests were performed using the YE-2000 type of hydraulic machine. The load on the platen was acquired using the SmartTest Computer-controlled System. Video images were acquired using a digital camera. The distance from the camera to a specimen was around 5.0 m. All photographs are taken using a Sony Cybershot DSC-W5 digital camera with sensor resolution of 5.0 mega pixels. The above-mentioned camera was placed normal to the rock exposure to be mapped.

2.2 Displacement Field

2.2.1 Theory Background

Digital pictures of the specimen were evaluated with Particle Image Velocimetry (PIV). The displacement is inferred from two consecutive images in a video. Both images are first divided into sub-windows respectively. The sub-window in the first image is then compared with one in the second image. The sum of the squared difference between the sub-windows is used as a criterion to define which sub-window is the "least unlike" one. The local displacement vectors are calculated for small sub-windows by cross-correlation, yielding a spatial average vector over the sub-window. The highest value in the correlation plane was used as an estimation of the displacement.

2.2.2 Computing Displacements

The video images were interrogated in a multi pass using different sizes of sub-windows with different overlaps. The calculation starts with relatively large sub-windows and refines the calculation using smaller ones. We start off with 64×64 large image, end with 16×16 after 6 iterations, and use 75% overlap of the sub-windows. The Signal-To-Noise ratio, Peak Height, Global, and Local filters were used to remove spurious vectors.

Fig. 1 represents the displacement fields before and after filtering. It can be seen that the distributions and values almost remain unchanged but the changes in any locations were more smoothly for the displacements after filtering.

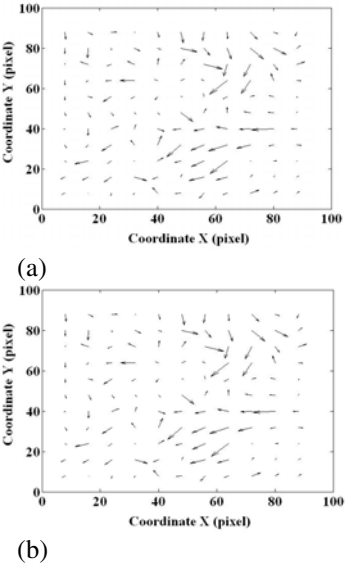

Fig. 1 Displacement field before and after filtering correction with (a) Before and (b) After corrections

The maximum correlation coefficient was computed in the sub-pixel level, and the Gaussian fit was utilized to estimate the displacements in the adjacent area of a point. The sub-pixel position was determined using the maximum value of the correlation coefficients computed by

$$x_0 = i + \frac{\ln R(i-1, j) - \ln R(i+1, j)}{2\ln R(i-1, j) - 4\ln R(i, j) + 2\ln R(i+1, j)}$$

$$y_0 = j + \frac{\ln R(i, j-1) - \ln R(i, j+1)}{2\ln R(i, j-1) - 4\ln R(i, j) + 2\ln R(i, j+1)}$$

where $R(i,j)$ is the maximum of the correlation coefficient matrix with the coordinates i and j; and $R(i\text{-}1, j)$, $R(i\text{+}1, j)$, $R(i, j\text{-}1)$, and $R(i, j\text{+}1)$ are the coefficients adjacent to $R(i,j)$ in the matrix.

3 Computation of Strain Field

The strain field was computed using the least square method for the discrete displacements. For an arbitrary point in the displacement field, fit the total m of the displacements around the point into a line. The slope of the line was considered as

the derivative in the direction of the line. The weights were applied to these derivatives. The weighted values were considered as the strain at this point. The full-field strain was obtained after conducting this process iteratively for each point.

Only the specimen DY2-2 is herein taken as an example to present the displacement and strain distributions. Three points on the surface of the specimen were selected as tracked ones to record the strain changes at different times. Fig. 2 is the location of the points. Figs. 3-5 represent the changes with time for these 3 points, respectively of the normal strain ε_x in the x-direction, the normal strain ε_y in the y-direction, and the rotation γ_{xy}.

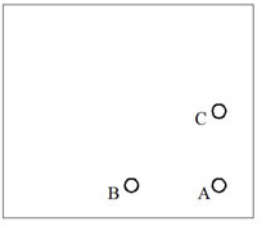

Fig. 2 Schematic diagram of three tracking points

In Fig. 3, most of ε_x were relatively small prior to 67 second; there was a sharply change at 67 second with a sharp increase in compressive strain only at point A and in tensile strain at points B and C. In Fig. 4, most of ε_y were relatively small characterized as tensile strains, prior to 65 second; at 65 second; there were a sharply change at all three points and a sharp increase in compressive strain only at the point A; the strains also fall into a chaos state after 65 second. In Fig. 5, most of the rotation γ_{xy} were relatively small prior to 65 second; there was a sharp change in the negative rotation at 65 second and a lot of changes occurred after that time at point A; while the rotations were more steadily at points B and C. From Figs. 3-5, it can be summarized that the types and values of the strains at different time have different features, depending on their locations at the specimen. The failure of a specimen did not occur at once but in a gradual way.

Fig. 6 presents the contour map of the normal strain field of the specimen at 3.0 and 17.0 seconds. It can be seen that the normal strain ε_x is unevenly distributed; the left and right parts of the specimen were respectively subjected to the

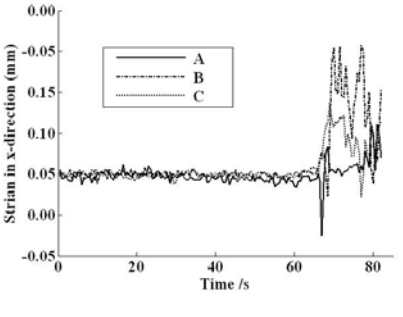

Fig. 3 Changes of normal strain ε_x in x-direction for three tracking points

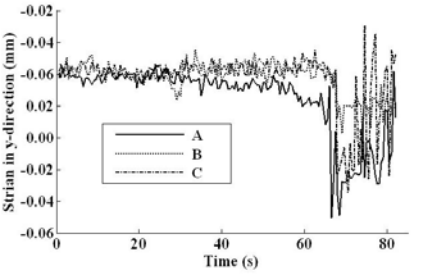

Fig. 4 Changes of normal strain ε_y in y-direction for three tracking points

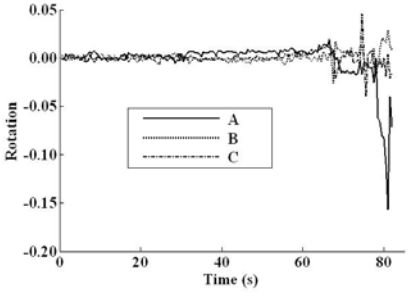

Fig. 5 Changes of the rotation γ_{xy} for three tracking points

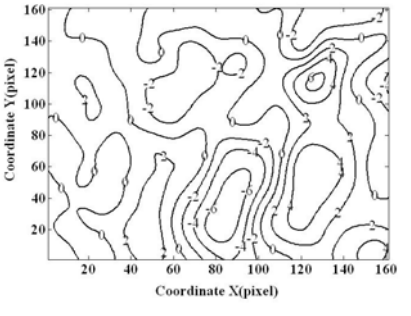

(a)

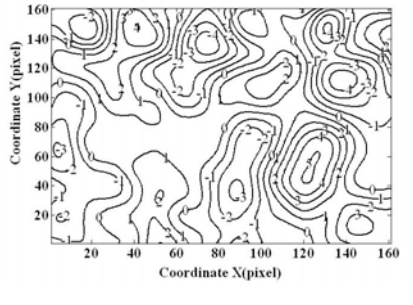

(b)

Fig. 6 Normal strain (×10-3) in x-direction, respectively (a) at 3.0 second; and (b) at 17.0 second

compressive and tensile loads until the specimen failures. This agrees with the fact that the right part of the specimen had the original cracks and easily to be stretched. From Fig. 6, it also can be seen that several strain concentration bands exist; and micro-cracks can not be seen or do not exist in some bands.

4 Summary

1. Using the video images captured during the uniaxial compression test, the full-field displacements and strains at any time and at any locations were obtained by using the particle image velocimetry technique. Many factors, such as the instabilities of the surroundings, influenced the accuracy of the displacements.
2. The types and values of the strains at different time have different features, depending on their relative locations at the specimen. The failure of a specimen did not occur at once but in a gradual way.
3. The normal strains were unevenly distributed, depending on the locations at the specimen and the types of the stresses. Several strain concentration bands may exist but did not definitely develop into micro-cracks.

Acknowledgements. Financial supports for the current study were provided by the Natural Sciences Foundation Committee of China (No.40972191) and the Shanghai Municipal Education Commission (No.09YZ39). These supports were gratefully acknowledged.

References

1. Bouaynaya, N., Schonfeld, D.: On the optimality of motion-based particle filtering. IEEE Trans. Circ. & Syst. Video Tech. 19, 1068–1072 (2009)
2. Chen, Y., Yu, W., Huang, X.: Application of digital image processing for strain analysis by square grid method. J. Plast. Eng. 16, 182–186 (2009) (in Chinese)
3. Deb, D., Hariharan, S., Rao, U.M., Ryu, C.H.: Automatic detection and analysis of discontinuity geometry of rock mass from digital images. Comput. & Geosci. 34, 115–126 (2008)
4. White, D.J., Take, W.A., Bolton, M.D.: Soil deformation measurement using particle image velocimetry (PIV) and photogrammetry. Géotech. 53, 619–631 (2003)
5. Xu, J., Zhao, X., Liu, B.: Digital image analysis of fluid inclusions. Int. J. Rock Mech. & Min. Sci. 44, 942–947 (2007)
6. Yin, X., Dang, F., Ding, W., Chen, H.: Morphologic measurement of crack in CT images of rock and soil. Chin. J. Rock Mech. & Eng. 25, 539–544 (2006) (in Chinese)